Editors' Suggestion

Asymmetric ferroelectricity by design in atomic-layer superlattices with broken inversion symmetry

Maitri P. Warusawithana,[1,*] Caitlin S. Kengle,[1] Xun Zhan,[2,3] Hao Chen,[2,3] Eugene V. Colla,[4] Michael O'Keeffe,[5] Jian-Min Zuo,[2,3] Michael B. Weissman,[4] and James N. Eckstein[3,4]

[1]*Department of Physics, University of North Florida, Jacksonville, Florida 32224, USA*

[2]*Department of Materials Science and Engineering, University of Illinois at Urbana-Champaign, Urbana, Illinois 61801, USA*

[3]*Materials Research Laboratory, University of Illinois at Urbana-Champaign, Urbana, Illinois 61801, USA*

[4]*Department of Physics, University of Illinois at Urbana-Champaign, Urbana, Illinois 61801, USA*

[5]*School of Molecular Sciences, Arizona State University, Tempe, Arizona 85287, USA*

(Received 20 March 2018; revised 21 May 2019; accepted 21 July 2021; published 4 August 2021)

In atomic-layer superlattices constructed using three constituent phases, $CaTiO_3$, $SrTiO_3$, and $BaTiO_3$, the stacking sequence of the atomic layers is found to control the symmetry of the high-temperature dielectric response. In such a superlattice when a nanostructured asymmetric strain is *programmed into the lattice* via the stacking order, the natural symmetry at high temperatures is removed and a polarized sample is obtained in which the polarization increases as the temperature is lowered. In contrast to a ferroelectric characterized by a bistable ground state with two *equal and opposite* electronic polarizations, our experiments show evidence of asymmetric ferroelectric correlations that set in when such a sample becomes hysteretic below a temperature T_x, with two *unequal* polarization states. We further show that both the magnitude and direction of this ferroelectric asymmetry can be controlled by the engineered atomic-layer stacking order and periodicity of the superlattice.

DOI: 10.1103/PhysRevB.104.085103

I. INTRODUCTION

Electronically polarized materials have broken inversion symmetry in the direction of polarization. Such materials are useful for nonlinear electrodynamic and electromechanical applications [1–3] since the polarization leads to a second order dielectric susceptibility that does not exist in symmetric materials [4]. In a ferroelectric [5], the polarization is due to a collective distortion of the lattice below an ordering temperature [1]. The centrosymmetric phase that prevails above this ordering temperature dictates that the degree of polarization below the ordering temperature is *equal* in either spontaneously picked direction. The high-temperature centrosymmetric crystal structure of $BaTiO_3$, a well-known ferroelectric, is shown in Fig. 1(a). The schematic of its characteristic free energy versus polarization relationship $F(P)$, below the ordering temperature shown in Fig. 1(b), demonstrates the symmetry of a natural ferroelectric ground state with two *equal and opposite* polarization levels. Many studies have explored the use of epitaxial strain to enhance polarization in such ferroelectric thin films [6–10]. Here we present a study in which nanostructured epitaxial strain programmed into the crystal, by design, fundamentally alters the free energy landscape of a ferroelectric as schematized in Fig. 1(c). This epitaxial strain as evidenced in x-ray diffraction reciprocal space maps [Fig. 1(e)] causes the constituent phases that comprise the superlattice to be clamped in plane to the substrate lattice constant. This results in changes to the out of plane lattice constant of each constituent phase, creating a built-in broken inversion symmetry in the out of plane direction as demonstrated by the asymmetrically distorted octahedra in Fig. 1(d). Our unique electrical measurements provide experimental insight as to what transpires in such a sample when collective order sets in starting from a high-temperature phase that lacks inversion symmetry. In contrast to that of a ferroelectric, the *asymmetric* two-state response we report here is consistent with local minima in $F(P)$ as schematically shown in Fig. 1(c), subject to a built-in asymmetric strain field.

II. RESULTS

Complex oxide materials, in particular, perovskites, show a wide range of physical properties in isostructural phases [11]. This structural compatibility allows pure molecular monolayers of different oxide phases to be stacked to form single-crystal superlattices with programmed supercell architecture [12–18]. In such atomic-layer superlattices, mechanical and electronic properties such as strain differences and charge transfer between different layers must be resolved at all of the heterointerfaces. If the layers are thin enough, modified aggregate properties emerge that are not present in any of the components individually [12,14–20]. Constructing such superlattices consisting of dielectric and ferroelectric phases has been explored as a means to obtain enhanced polarization [21–24]. In this work strained atomic-layer superlattices at the ultimate monolayer limit are constructed using dielectric and ferroelectric titanate phases, $CaTiO_3$ (CTO), $SrTiO_3$ (STO), and $BaTiO_3$ (BTO), which in bulk have different lattice constants, BTO > STO > CTO. The stacking sequence of the molecular layers controls the symmetry of the strain field along the stacking direction. Theoretical analysis by Sai *et al.* [19] has shown that structural relaxation

*maitriw@unf.edu

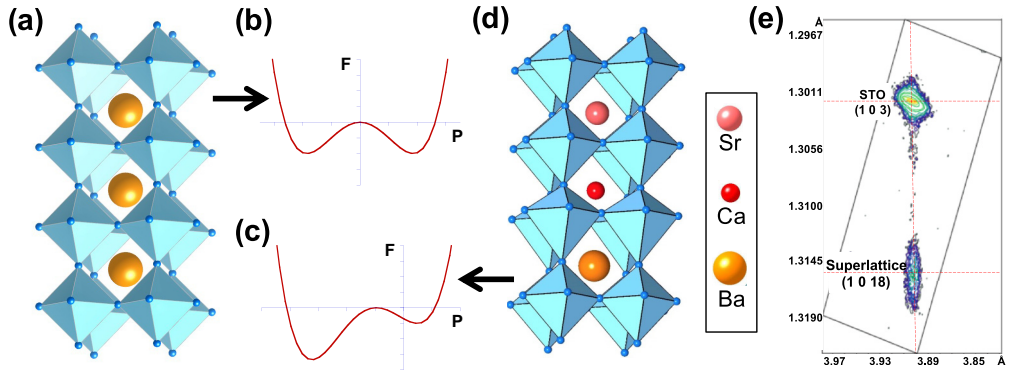

FIG. 1. Natural ferroelectricity and asymmetric ferroelectricity by design. (a) Centrosymmetric crystal structure of $BaTiO_3$ above the ferroelectric ordering temperature. (b) The characteristic free energy landscape for the ground state of a ferroelectric. (c) Schematic of an engineered free energy landscape for the ground state of an asymmetric ferroelectric: a noncentrosymmetric crystal that, at low temperatures, develops bistable correlations subject to a built-in asymmetric strain field. $F(P)$ shown here is consistent with a "–" stacking sequence. (d) A noncentrosymmetric crystal by design: bond valence sum calculations of the crystal structure for a 111− superlattice indicating distortions in the Ti-O octahedra along the stacking direction. (e) X-ray diffraction reciprocal space map of a 222+ superlattice around the substrate STO (103) peak indicating that the superlattice is clamped to the in-plane substrate lattice constant. Red dashed lines are a guide to the eye.

of such dielectric superlattices with built-in asymmetry leads to an asymmetric energy versus polarization relation. More recent theoretical work indicates that such asymmetric superlattices should show two unequal polarization states [25,26] along the superlattice stacking direction. The temperature-dependent data we report here are qualitatively consistent with the calculated zero-temperature energy landscape [19] and the predicted direction of asymmetry [25,27].

Figure 2(a) shows the overall structure of the samples we studied. In each sample a superlattice with a specific supercell architecture was sandwiched between conducting $La_{0.7}Sr_{0.3}MnO_3$ (LSMO) layers [28] that were fully strained to the (001) STO substrate, providing the devices with symmetric top and bottom electrodes [29]. Supercells with broken inversion symmetry are indicated with a "+" or "–" designation [Fig. 2(c)]: A stacking sequence of BTO → STO → CTO is designated + and the reverse sequence is designated −; i.e., a superlattice with repeating supercells where each supercell consists of six molecular layers of BTO followed by two layers of STO and two layers of CTO is denoted 622+. There is no + or − designation for the 1212 superlattice, as it preserves inversion symmetry. The superlattices were assembled using ozone-assisted molecular beam epitaxy [29–31] by sequentially growing individual molecular layers of the specified titanate phases at 720 °C and an ozone pressure of 5×10^{-7} Torr. Each superlattice was started and ended with the CTO block to ensure identical interfaces to the base and top LSMO electrodes for all samples studied [29].

To verify the growth of the asymmetric structures, cross sectional *Z*-contrast scanning transmission electron microscopy (STEM) [32] was carried out on superlattices cut perpendicular to in-plane Ti-O bond directions. A STEM image obtained using a JEOL 2010F microscope for a 111− superlattice is shown in Fig. 2(b). The image shows the

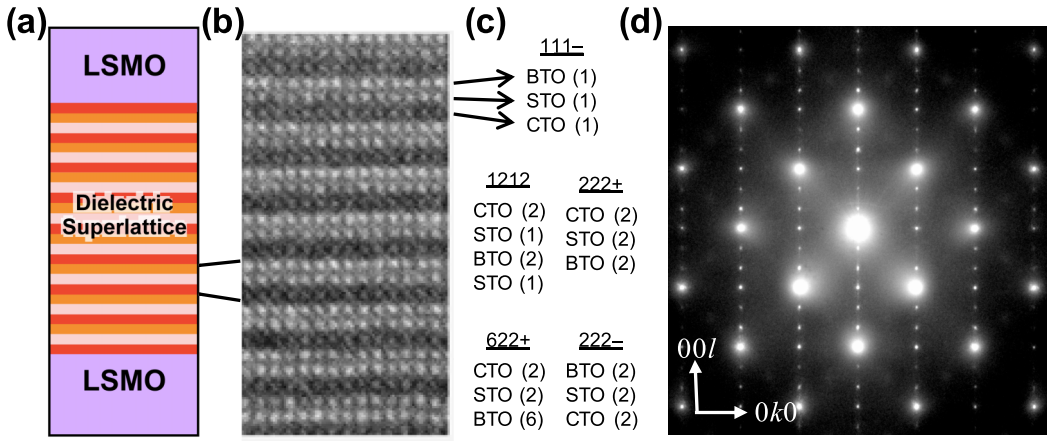

FIG. 2. Sample architectures and imaging the commensurately strained sequenced superstructure. (a) Overall structure of capacitor devices that include a dielectric superlattice in between two conducting manganite layers. (b) STEM image of a 111− superlattice grown directly on an STO substrate. (c) Some of the supercell architectures we studied. (d) Electron diffraction pattern of a 111− superlattice on a logarithmic intensity scale. Sharp superlattice spots verify sequenced superstructure that is commensurately strained to the substrate: The asymmetric stacking sequence results in an asymmetric strain field along the stacking direction.

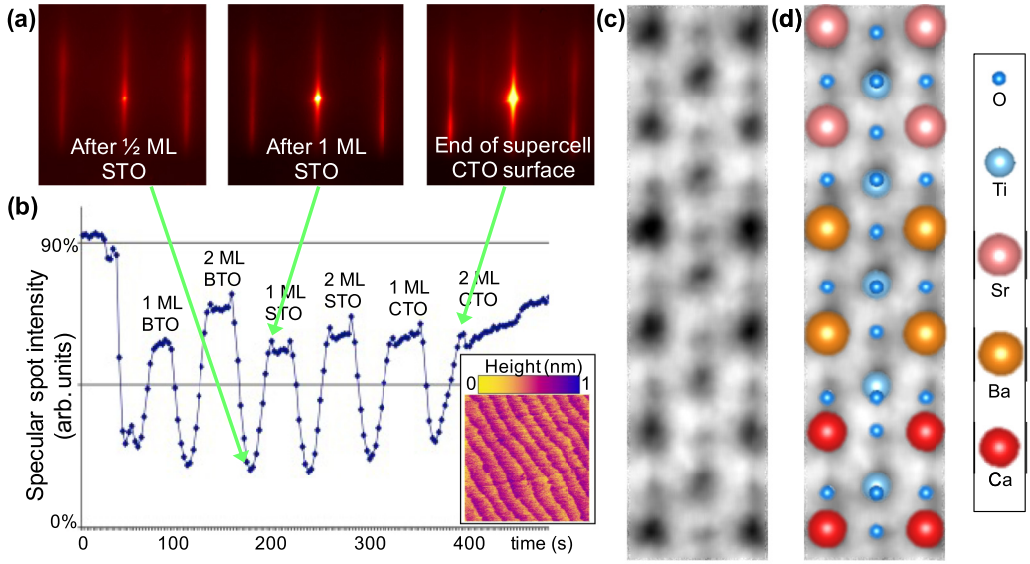

FIG. 3. Evidence for sharp two-dimensional (2D) interfaces and octahedral distortions due to asymmetric strain. (a) Representative RHEED images at different stages of growth of a 222+ superlattice. (b) Self-organized oscillations of the RHEED specular intensity recorded *in situ* during deposition of a 222+ supercell. The plateaus in intensity at the end of each molecular layer correspond to a short (∼25 s) anneal. These plateaus suggest the lack of surface kinetics that could cause interface roughening. Inset shows an *ex situ* AFM image (1 μm square) of the surface of a 222+ superlattice. (c) Bright-field atomic-resolution STEM image of a 222+ superlattice shows the average lattice positions of all the atoms including oxygen. Asymmetric displacements of the oxygen sublattice with respect to the *A*-site sublattice can be observed. (d) Bond valence sum calculated atomic positions for a 222+ superlattice superimposed on the STEM image of (c) indicate qualitative agreement between calculated and observed lattice positions.

programmed layering structure. Electron diffraction patterns for this 111− sample recorded along the [100] zone axis [Fig. 2(d)] show sharp superlattice spots with ∼one-third the period of STO reflections along the [00l] direction, indicating good overall homogeneity of the sequenced superstructure (see Supplemental Material [29] for a simulation). Furthermore, diffraction spots in the [0k0] direction indicate that the superlattice is clamped to the substrate as was also revealed by x-ray diffraction reciprocal space maps of similar samples. The reciprocal space map for a 222+ superlattice sample around the STO (103) peak is shown in Fig. 1(e). The data show that the film is pseudomorphic with the substrate with an in-plane lattice constant of 3.905 Å and an out of plane superlattice constant of 23.664 Å. With all three components of the superlattice, BTO, STO, and CTO, clamped to the substrate, the degree of in-plane biaxial strain at each heterointerface varies, resulting in an out of plane strain gradient that mimics the symmetry of the structure. With the film clamped to the substrate, the local bond strain is controlled by the superlattice architecture: Stacking architectures breaking inversion symmetry lead to asymmetric strain gradients in the z direction that are tuned by the precise supercell structure. Figure 1(d) shows a model structure of a 111− sample constructed from bond valence sum [33,34] calculations [29]. The asymmetrically distorted Ti-O octahedra in the model are a consequence of the asymmetry of the structure and predict a polarized material.

During the growth of each superlattice, the growth surface was monitored *in situ* using reflection high-energy electron diffraction (RHEED). Throughout each superlattice, the growth surface exhibited RHEED patterns [Fig. 3(a)] that indicated a strictly two-dimensional, Frank–Van der Merwe [35] growth mode. Strong RHEED oscillations were observed for each unit cell grown [12,36], whether the growth occurred on top of the same material or a different phase [see Fig. 3(b)], implying that the heterointerfaces were two dimensional and no significant roughening occurred to degrade the interfacial strain engineering. The flatness inferred from the sharpness of the RHEED specular reflection quantitatively agrees with that determined by postgrowth atomic force microscopy [Fig. 3(b) inset], which showed atomically flat terraces, >100 nm wide, with one unit cell high, ∼0.4 nm, steps between terraces and an rms roughness of <1.5 Å.

We further probed the asymmetric lattice distortions using atomic-resolution STEM. Figure 3(c) shows an image of a 222+ superlattice sample obtained using a Themis Z microscope with an annular bright-field detector for small angle scattering, which is sensitive to light atoms [29]. The Z contrast of the image not only allows locating the heavier atoms but also allows identifying the average locations of the oxygen atoms in the lattice. Asymmetric displacements of the oxygen sublattice relative to the sequenced *A*-site sublattice can be observed in the STEM image (see also [29]). In Fig. 3(d) we superimpose a model structure of the 222+ sample constructed from bond valence sum calculated lattice coordinates [29] with the STEM image of Fig. 3(c). Although the average position of atoms imaged by STEM does not allow for quantitative measurements of the lattice distortions (nor is this the scope of our current work), the observed asymmetric displacements of the atoms qualitatively agree with the calculated atomic positions. These asymmetric displacements are built into the sample by design and provide

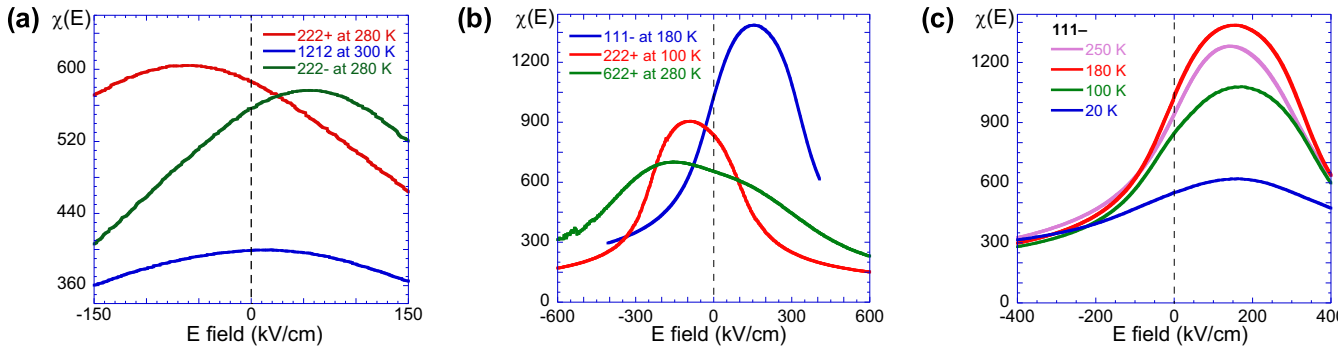

FIG. 4. Field tuning of the dielectric susceptibility for different superlattices. These measurements were made at 77 Hz. (a) Data from the 222+, 1212, and 222− samples around room temperature showing the effect of structural symmetry on the symmetry of the electronic response. (b) Data from the asymmetric superlattices, 222+, 622+, and 111−, near the temperature which maximizes χ in each case. (c) $\chi(E)$ for the 111− superlattice at different temperatures.

the necessary condition for polarization along the stacking direction.

To directly probe the susceptibility and polarization of the dielectric superlattice samples, the heterostructures were processed into parallel-plate capacitor devices [29]. Capacitance measurements were obtained by measuring the complex current and voltage across the capacitor simultaneously by two lock-in amplifiers. Field tuning of the dielectric susceptibility, $\chi(E)$, was obtained from low-frequency (7–770 Hz) capacitance measurements made with a superimposed dc bias field [29] at temperatures from 4.2 to 400 K. The very low values obtained for the zero-bias loss tangent, $\tan\delta$ <0.007 at 300 K for all devices studied, confirmed the quality of the samples [37–39]. The susceptibility around room temperature of the set of three superlattices 222+, 1212, and 222−, which had the same total number of unit cells of each titanate component (and identical electrode interfaces), is shown in Fig. 4(a). The $\chi(E)$ of these three samples unambiguously demonstrates the effect of the built-in asymmetry on the high-temperature dielectric response. As found before [12], the symmetric sample, 1212, has an approximately symmetric $\chi(E)$ curve, while the 222+ and 222− structures show similar curves that are oppositely displaced by an effective polarizing field, E_p, originating in the asymmetric strain due to the stacking order. The sign of E_p is determined by the sign of the stacking asymmetry. Figure 4(b) shows data from the 111−, 222+, and 622+ samples at the temperature which in each case maximizes the susceptibility. The shape of $\chi(E)$ for the 622+ sample is distinctly different from the shape of $\chi(E)$ for the shorter period superlattices, 111− and 222+. The former is not a symmetric function when reflected about the peak of the susceptibility—this could be due to different populations of dipoles, the origin of which could be related to the thicker (six unit cells) BTO block in each supercell. The variation observed in the shape of $\chi(E)$ demonstrates the degree to which nanoscopic strain field engineering through programmed superlattice structure can control the dielectric response in such samples.

The oppositely shifted $\chi(E)$ curves observed for samples 222+ and 222− and the symmetric $\chi(E)$ curve observed for the 1212 sample [Fig. 4(a)] offer evidence to support that the identically constructed electrode interfaces [29] provide symmetric top and bottom contacts to the dielectric superlattice samples. This means that the 222+ sample is not any different from an upside-down 222− sample (i.e., if the electrical terminals were switched for the 222− sample, the response of the 222− sample would then be similar to the response of the 222+ sample). Similarly, if we constructed a 111+ sample, this would be an upside-down 111− sample and as such, a comparison of the resulting polarization of a pair of such samples will be deemed trivial. Therefore, to differentiate between the polarization response and any correlations that may arise at low temperatures due to opposite stacking asymmetry as well as the strength of the built-in asymmetric strain field, we deliberately chose to carry out further careful measurements on samples 111− and 222+.

For short enough period superlattices, i.e., 111± and 222±, the dielectric response is symmetric about E_p : $\chi = C(E–E_p)$, where $C(x)$ is a symmetric function of x (see Fig. 4(c) and [29]). We find that the aggregate dielectric response is due to the sum of a very nearly homogeneous set of dipoles plus a smaller field-independent elastic component [12,29]. While the larger component due to the two-state dipoles, Lorentzian in shape, saturates with applied E field and temperature [29], the much smaller elastic component does not saturate even at large E fields and low temperatures. If the total dielectric response $\chi(E)$ comes only from two-state dipoles that are polarized by E_p, the polarization at zero field, P_0, can be obtained from $P_0 \equiv P(E=0) = -\varepsilon_0 \int_0^{E_p} dE' \chi(E')$. Any contribution to P_0 due to the smaller elastic component, however, cannot be determined in a similar way. However, the elastic susceptibility is about one-tenth of the total, and we believe the uncertainty this adds to an estimate of P_0 is small [29]. The value of P_0 obtained in this manner for the 111− sample (at $T_{\rm ref} = 250$ K) is $-0.147 \pm 0.008\,{\rm C/m^2}$ and for the 222+ sample (at $T_{\rm ref} = 280$ K) is $+0.031 \pm 0.005\,{\rm C/m^2}$. While the sign of P_0 follows the sign of the stacking asymmetry of the samples, the magnitude of P_0 for the 111− sample is approximately a factor of 4 larger than that of the 222+ sample: The stronger strain gradients due to the shorter superlattice period of the 111− sample more effectively polarize the two-state dipoles.

This method of evaluating P_0 by integrating $\chi(E)$ is valid only at high temperatures [29]. At lower temperatures

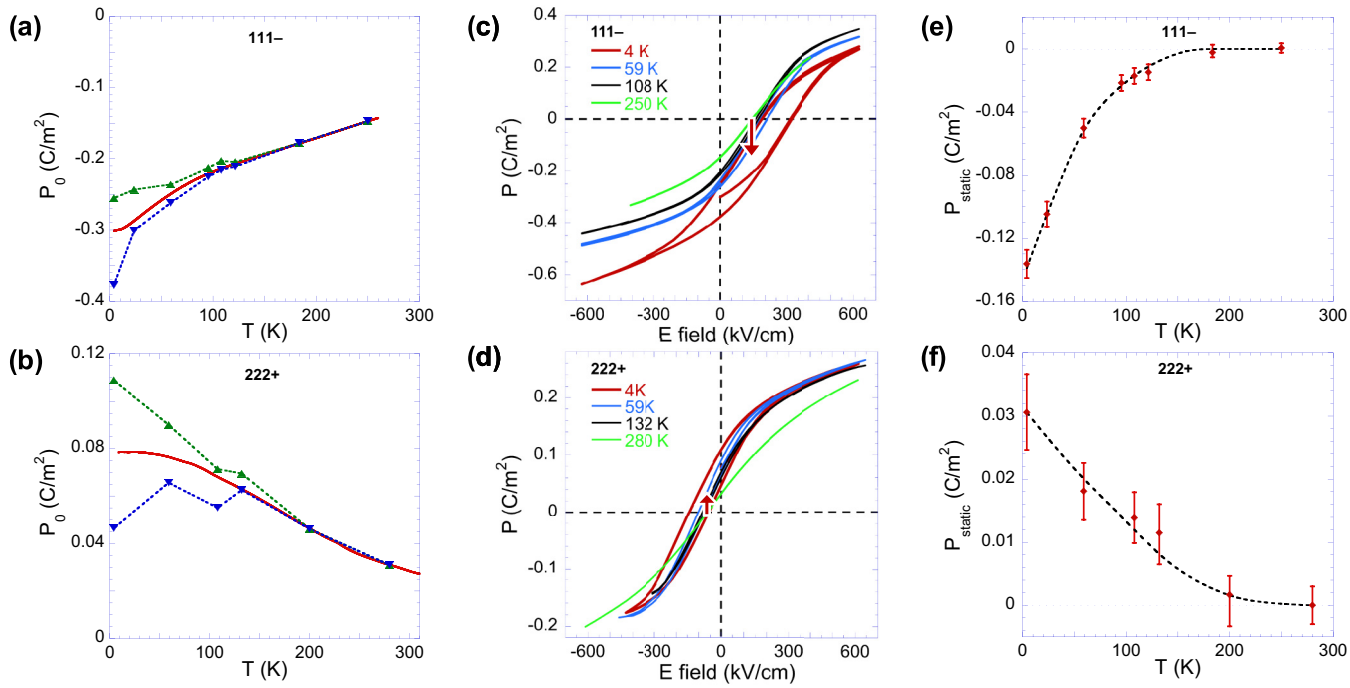

FIG. 5. Asymmetric ferroelectric state in the 111− and 222+ samples. $P_0(T)$ for (a) 111− sample and (b) 222+ sample obtained by pyrocurrent measurements (solid lines). The remanent polarization levels at zero bias are also indicated (connected by dotted lines). $P(E)$ curves at different temperatures for (c) 111− sample and (d) 222+ sample. In both samples the $P(E)$ curves show a constant shift from the origin at all temperatures along the E-field axis and a strong temperature-dependent shift below T_x along the polarization axis (indicated by an arrow). The locus of the symmetry point of the $P(E)$ curves for (e) 111− sample and (f) 222+ sample in the polarization-temperature plane showing the growth of P_{static}. The error bars indicate an estimate of the overall uncertainty. The shifts in $P(E)$ and the sign of $P_0(T)$ and $P_{\text{static}}(T)$ for the 222+ sample are opposite to that of the 111− sample.

the two-state dipole component of the dielectric response becomes slower than typical ac measurement frequencies [12,29]. Additionally, if long-range correlations occur, the slow kinetics could completely mask the collective growth of polarization at any practical measurement frequency. Alternatively, $[P_0(T)–P_0(T_{\text{ref}})]$ can be directly obtained by carefully measuring the pyrocurrent, I_p, starting from some reference temperature, T_{ref}. I_p is the product of the rate of change of polarization with temperature, dP_0/dT, and how fast the sample temperature is changed, dT/dt [29]. The total current measured consisted of I_p as well as a thermoelectric current, I_{TE}, which is only a function of temperature rather than of dT/dt. By measuring the total current while heating as well as cooling the device, I_p and I_{TE} can be separated, and I_p, of the order of a 100 fA for reasonable cooling and heating rates, was extracted well above the measurement noise level for both the 111− sample and the 222+ sample. Thus, $P_0(T)$ was obtained for the 111− sample and the 222+ sample by integrating I_p and setting $P_0(T_{\text{ref}})$ to the value found above by integrating the susceptibility at T_{ref} (250 K for the 111− sample and 280 K for the 222+ sample).

In both samples, we find that the magnitude of $P_0(T)$ increases continuously as the sample is cooled while the sign of $P_0(T)$ remains opposite for the 111− and 222+ samples. See Figs. 5(a) and 5(b) (solid lines). Internal asymmetric strain gradients become increasingly effective at biasing the dipole component as the temperature is lowered. This field-free cooling is similar to electric field cooling a paraelectric [1], where E_p plays the role of an applied electric field. The overall increase in the magnitude of $P_0(T)$, from ∼250 K down to 4 K, however, is approximately a factor of 4 larger for the 111− sample than that for the 222+ sample. For comparison, the zero-field polarization, $P_0(4\,\text{K}) = -0.301 \pm 0.009\,\text{C/m}^2$ for the 111− sample and $P_0(4\,\text{K}) = +0.078 \pm 0.005\,\text{C/m}^2$ for the 222+ sample. Furthermore, an increase in the growth rate of polarization, $|dP_0/dT|$, is observed at $T_x \approx 110\,\text{K}$ in the 111− sample. See Fig. 5(a) and [29]. This is coincident with the onset of long-range ferroelectric correlations as evidenced by the onset of polarization hysteresis [Fig. 5(c)]. For the 222+ sample, however, no such clear increase in $|dP_0/dT|$ can be observed in Fig. 5(b). This could be due to the weaker temperature dependence of P_0 for the 222+ sample. Nevertheless, polarization hysteresis is still observed in the 222+ sample [see Fig. 5(d)] below a temperature $T_x \approx 132\,\text{K}$.

To probe the state of the 111− and the 222+ superlattices below T_x, and to obtain $P(E)$ avoiding complications due to slow kinetics, we carried out a dc-transient measurement scheme (see Supplemental Material for measurement details [29]). This involved stepping the dc bias and integrating the transient current across a 10 GΩ resistor to obtain $P(E)$. The device size and geometry of the 111− and the 222+ sample capacitors gave an RC time constant (τ) on the order of 6 s. At each step of the dc bias, the transient current was integrated for well over 10τ to obtain the full response. The value of P_0 at each temperature, obtained from Fig. 5(a) (solid line)

for the 111− sample and Fig. 5(b) (solid line) for the 222+ sample, provided the starting polarization for each $P(E)$ curve. The $P(E)$ curves obtained at high temperatures (i.e., ∼250 K) by this dc technique compared well with that obtained by ac capacitance measurements, confirming the accuracy of this dc-transient measurement scheme. To avoid sample poling, each $P(E)$ curve was obtained after cooling from well above T_x.

Figures 5(c) and 5(d) show the unusual polarization hysteresis that emerges as ferroelectric correlations set in subject to the programmed asymmetric strain of the 111− and the 222+ samples. Above T_x, $P(E)$ is like that of a paraelectric, although shifted along the E-field axis due to the presence of E_p arising from the built-in strain gradients: $P(E)$ for the 111− sample is shifted in the $+E$ direction [Fig. 5(c)] while $P(E)$ for the 222+ sample is shifted in the $-E$ direction [Fig. 5(d)]. Below T_x, a hysteresis loop opens up in both samples. The points of interception of these loops with the $E = 0$ axis give the two polarization states at zero field and are indicated, connected by dotted lines, in Figs. 5(a) and 5(b) for the 111− and the 222+ samples, respectively. We find the temperature T_x at which the bistability emerges is similar for both samples: $T_x \approx 132$ K for the 222+ sample and $T_x \approx 110$ K for the 111− sample. This onset temperature of hysteresis is related to the strength of a polarization instability. While asymmetric strain gradients may, in fact, work to suppress such polarization instability, other factors like the strain state of each molecular layer and the thickness of each constituent block of the superlattice may contribute to the instability.

Most interestingly, below T_x the loops are displaced in an unusual manner in the P-E plane. For each $P(E)$ curve we can observe a symmetry point for simultaneous inversions of E and P. Above T_x the symmetry point is roughly temperature independent at $P = 0\,\mathrm{C/m^2}$ and $E = E_p$, where $E_p = +150 \pm 10\,\mathrm{kV/cm}$ for the 111− sample and $E_p = -65 \pm 15\,\mathrm{kV/cm}$ for the 222+ sample: The effective polarizing field simply biases the two-state dipoles. Below T_x, the symmetry point occurs at the same E field, E_p. However, since the value of P at the symmetry point is a strong function of T, the $P(E)$ curves shift along the polarization axis direction by a static polarization offset, P_{static}, indicated by an arrow in Figs. 5(c) and 5(d). This temperature-dependent offset, $P_{\mathrm{static}}(T)$, is plotted in Figs. 5(e) and 5(f) for the 111− and the 222+ samples, respectively. At low temperatures, $P_{\mathrm{static}}(4\,\mathrm{K}) = -0.136 \pm 0.013\,\mathrm{C/m^2}$ for the 111− sample and $P_{\mathrm{static}}(4\,\mathrm{K}) = +0.031 \pm 0.006\,\mathrm{C/m^2}$ for the 222+ sample: The magnitude of P_{static} is about a factor of 4 larger for the 111− sample and the sign of P_{static} is determined by the sign of the stacking asymmetry. The dc measurement technique we used [29] made sure that the shift in the $P(E)$ curves observed along the polarization direction can only be due to a *real* static polarization. This P_{static} we observe is entirely different from the *dynamic* polarization offset [40] that has been reported in materials exhibiting asymmetric or rectifying leakage conductance as a function of voltage when measured using conventional techniques [41] or the offset in hysteresis observed along the E-field direction that has been attributed to a population of defects [42].

III. DISCUSSION

The *static* electronic polarization offset we report here is a property of the thermodynamic state of the asymmetric superlattices we constructed. It is unlike that of any known natural system and arises only because of the atomic-scale asymmetric strain engineered into the sample. In particular, the polarization below T_x is not what would be obtained for an ordinary ferroelectric material subject to a built-in polarizing field. In that case the hysteretic $P(E)$ loop would be shifted in E, but not in P. The two branches would have the same $|P|$ at points reflected through the loop's symmetry point, with equal magnitude of the positive and negative saturation polarizations. However, in this engineered crystal, the magnitude of the saturation polarization of the upper branch is smaller (larger) and that of the lower branch is larger (smaller) for the 111− sample (222+ sample), shifted by a temperature-dependent P_{static} that sets in only in the regime with ferroelectric correlations. It is also interesting to note that while E_p scales roughly linearly with the inverse supercell thickness (three unit cells for 111− and six unit cells for 222+), P_{static} and P_0 scale roughly quadratically with the inverse supercell thickness.

The detailed origin of P_{static} is not fully understood. In particular, the P_{static} we find is considerably larger (a factor of 10) than the zero-temperature prediction [25]. It may be due to a permanent polarization of the smaller elastic component that arises below T_x which adds a *nonswitchable* polarization to the polarization of the two-state dipoles. Alternatively, it may be due to a change of the two-dipole states themselves. To explain our observation, such changes would need to arise in the model only when collective order sets in, subject to the influence of the asymmetric strain field introduced by the layering architecture.

This unique asymmetric ferroelectricity we observe having two unequal polarization states describes a qualitatively different class of materials which may have unexpected applications. For example, it may be possible to choose the value of P_{static} so that one of the two polarization states actually has zero polarization and properties such as the nonlinear electromagnetic susceptibility or piezoelectric response could be turned on and off by switching between states. We hope this work will trigger further experimental and theoretical investigations that will not only lead to a quantum understanding of this asymmetric ferroelectric state but also harness the potential of symmetry breaking at the atomic scale to obtain nanostructured materials with tailored electronic properties by design.

ACKNOWLEDGMENTS

We thank D. Vanderbilt, R. Martin, D. G. Schlom, and L. Chao for useful discussions and M. Vissers for help with data acquisition. The work carried out at the University of Illinois at Urbana-Champaign was supported by the US Department of Energy, Division of Materials Sciences DEFG02-91ER45439 and the National Science Foundation NSF EIA00-81437. M.P.W. was supported by the University of North Florida, Faculty Development Scholarship Grant.

[1] M. E. Lines and A. M. Glass, *Principles and Applications of Ferroelectrics and Related Materials* (Clarendon Press, Oxford, 1977).

[2] *Guided Wave Nonlinear Optics*, NATO Science Series E Vol. 214, edited by D. B. Ostrowsky and R. Reinisch (Kluwer, Dordrecht, 1992).

[3] D. L. Polla and L. F. Francis, Processing and characterization of piezoelectric materials and integration into microelectromechanical systems, Annu. Rev. Mater. Sci. **28**, 563 (1998).

[4] R. W. Boyd, *Nonlinear Optics* (Academic Press, Boston, 1992).

[5] A century of ferroelectricity, Nat. Mater. **19**, 129 (2020).

[6] K. J. Choi, M. Biegalski, Y. L. Li, A. Sharan, J. Schubert, R. Uecker, P. Reiche, Y. B. Chen, X. Q. Pan, V. Gopalan *et al.*, Enhancement of ferroelectricity in strained $BaTiO_3$ thin films, Science **306**, 1005 (2004).

[7] N. A. Pertsev, A. K. Tagantsev, and N. Setter, Phase transitions and strain-induced ferroelectricity in $SrTiO_3$ epitaxial thin films, Phys. Rev. B **61**, R825 (2000).

[8] J. H. Haeni, P. Irvin, W. Chang, R. Uecker, P. Reiche, Y. L. Li, S. Choudhury, W. Tian, M. E. Hawley, B. Craigo *et al.*, Room-temperature ferroelectricity in strained $SrTiO_3$, Nature **430**, 758 (2004).

[9] J. B. Neaton and K. M. Rabe, Theory of polarization enhancement in epitaxial $BaTiO_3/SrTiO_3$ superlattices, Appl. Phys. Lett. **82**, 1586 (2003).

[10] J. H. Lee, L. Fang, E. Vlahos, X. Ke, Y. W. Jung, L. F. Kourkoutis, J.-W. Kim, P. J. Ryan, T. Heeg, M. Roeckerath *et al.*, A strong ferroelectric ferromagnet created by means of spin-lattice coupling, Nature **466**, 954 (2010).

[11] R. H. Mitchell, *Perovskites: Modern and Ancient* (Almaz Press, Thunder Bay, Canada, 2002).

[12] M. P. Warusawithana, E. V. Colla, J. N. Eckstein, and M. B. Weissman, Artificial Dielectric Superlattices with Broken Inversion Symmetry, Phys. Rev. Lett. **90**, 036802 (2003).

[13] A. Palanisami, M. Warusawithana, J. N. Eckstein, M. B. Weissman, and N. D. Mathur, Role of disorder in phase coexistence in manganites: Noise in layered films, Phys. Rev. B **72**, 024454 (2005).

[14] A. Bhattacharya, X. Zhai, M. Warusawithana, J. N. Eckstein, and S. D. Bader, Signatures of enhanced ordering temperatures in digital superlattices of $(LaMnO_3)_m/(SrMnO_3)_{2m}$, Appl. Phys. Lett. **90**, 222503 (2007).

[15] A. Bhattacharya, S. J. May, S. G. E. te Velthuis, M. Warusawithana, X. Zhai, B. Jiang, J. M. Zuo, M. R. Fitzsimmons, S. D. Bader, and J. N. Eckstein, Metal-Insulator Transition and its Relation to Magnetic Structure in $(LaMnO_3)_{2n}/(SrMnO_3)_n$ Superlattices, Phys. Rev. Lett. **100**, 257203 (2008).

[16] C. Adamo, X. Ke, P. Schiffer, A. Soukiassian, M. Warusawithana, L. Maritato, and D. G. Schlom, Electrical and magnetic properties of $(SrMnO_3)_n(LaMnO_3)_{2n}$ superlattices, Appl. Phys. Lett. **92**, 112508 (2008).

[17] X. Zhai, C. S. Mohapatra, A. B. Shah, J.-M. Zuo, and J. N. Eckstein, New optical absorption bands in atomic-layer superlattices, Adv. Mater. **22**, 1136 (2010).

[18] E. Bousquet, M. Dawber, N. Stucki, C. Lichtensteiger, P. Hermet, S. Gariglio, J.-M. Triscone, and P. Ghosez, Improper ferroelectricity in perovskite oxide artificial superlattices, Nature **452**, 732 (2008).

[19] N. Sai, B. Meyer, and D. Vanderbilt, Compositional Inversion Symmetry Breaking in Ferroelectric Perovskites, Phys. Rev. Lett. **84**, 5636 (2000).

[20] G. Logvenov, A. Gozar, and I. Bozovic, High-temperature superconductivity in a single copper-oxygen plane, Science **326**, 699 (2009).

[21] H. N. Lee, H. M. Christen, M. F. Chisholm, C. M. Rouleau, and D. H. Lowndes, Strong polarization enhancement in asymmetric three-component ferroelectric superlattices, Nature **433**, 395 (2005).

[22] M. Dawber, C. Lichtensteiger, M. Cantoni, M. Veithen, P. Ghosez, K. Johnston, K. M. Rabe, and J.-M. Triscone, Unusual Behavior of the Ferroelectric Polarization in $PbTiO_3/SrTiO_3$ Superlattices, Phys. Rev. Lett. **95**, 177601 (2005).

[23] M. Dawber, N. Stucki, C. Lichtensteiger, S. Gariglio, P. Ghosez, and J.-M. Triscone, Tailoring the properties of artificially layered ferroelectric superlattices, Adv. Mater. **19**, 4153 (2007).

[24] E. Khestanova, N. Dix, I. Fina, M. Scigaj, J. M. Rebled, C. Magén, S. Estradé, F. Peiró, G. Herranz, J. Fontcuberta *et al.*, Untangling electrostatic and strain effects on the polarization of ferroelectric superlattices, Adv. Funct. Mater. **26**, 6446 (2016).

[25] S. M. Nakhmanson, K. M. Rabe, and D. Vanderbilt, Polarization enhancement in two- and three-component ferroelectric superlattices, Appl. Phys. Lett. **87**, 102906 (2005).

[26] S. M. Nakhmanson, K. M. Rabe, and D. Vanderbilt, Predicting polarization enhancement in multicomponent ferroelectric superlattices, Phys. Rev. B **73**, 060101(R) (2006).

[27] Y.-C. Gao, C.-G. Duan, X. D. Tang, Z. G. Hu, P. Yang, Z. Zhu, and J. Chu, A first-principles study on the intrinsic asymmetric ferroelectricity of the $SrTiO_3-BaTiO_3-CaTiO_3$ tricolor superlattice at the nanoscale, J. Phys.: Condens. Matter **25**, 165901 (2013).

[28] J. O'Donnell, A. E. Andrus, S. Oh, E. Colla, M. Warusawithana, B. A. Davidson, and J. N. Eckstein, Growth of "colossal" magnetoresistance heterostructures by molecular beam epitaxy, Magnetoresist. Oxides Relat. Mater. **602**, 9 (2000).

[29] See Supplemental Material at http://link.aps.org/supplemental/10.1103/PhysRevB.104.085103 for information on MBE growth of heterostructures and device fabrication, bond valence sum calculations, atomic-resolution imaging, dipole and elastic components of susceptibility, and electronic measurement techniques used.

[30] J. N. Eckstein and I. Bozovic, High-temperature superconducting multilayers and heterostructures grown by atomic layer-by-layer molecular beam epitaxy, Annu. Rev. Mater. Sci. **25**, 679 (1995).

[31] J. N. Eckstein, M. Zheng, X. Zhai, B. Davidson, M. Warusawithana, and S. Oh, in *Molecular Beam Epitaxy* (Elsevier, Oxford, 2013), pp. 509–528.

[32] S. J. Pennycook, *Z*-contrast stem for materials science, Ultramicroscopy **30**, 58 (1989).

[33] I. D. Brown, *The Chemical Bond in Inorganic Chemistry: The Bond Valence Model* (Oxford University Press, Oxford, 2006).

[34] N. E. Brese and M. O'Keeffe, Bond-valence parameters for solids, Acta Crystallogr., Sect. B **47**, 192 (1991).

[35] D. W. Pashley, Epitaxy growth mechanisms, Mater. Sci. Technol. **15**, 2 (1999).

[36] J. H. Haeni, C. D. Theis, and D. G. Schlom, RHEED intensity oscillations for the stoichiometric growth of $SrTiO_3$ thin films by reactive molecular beam epitaxy, J. Electroceram. **4**, 385 (2000).

[37] A. R. James and X. X. Xi, Effects of buffer layer thickness and strain on the dielectric properties of epitaxial $SrTiO_3$ thin films, J. Appl. Phys. **92**, 6149 (2002).

[38] M. Nayak and T.-Y. Tseng, Dielectric tunability of barium strontium titanate films prepared by a sol-gel method, Thin Solid Films **408**, 194 (2002).

[39] M. Jain, S. B. Majumder, R. S. Katiyar, F. A. Miranda, and F. W. Van Keuls, Improvement in electrical characteristics of graded manganese doped barium strontium titanate thin films, Appl. Phys. Lett. **82**, 1911 (2003).

[40] J. V. Mantese, Comment on "Graded ferroelectric thin films: Possible origin of the shift along the polarization axis" [Appl. Phys. Lett. **81**, 5015 (2002)], Appl. Phys. Lett. **83**, 809 (2003).

[41] G. Poullain, R. Bouregba, B. Vilquin, G. Le Rhun, and H. Murray, Response to "Comment on 'Graded ferroelectric thin films: Possible origin of the shift along the polarization axis"', Appl. Phys. Lett. **83**, 811 (2003).

[42] A. R. Damodaran, E. Breckenfeld, Z. Chen, S. Lee, and L. W. Martin, Enhancement of ferroelectric Curie temperature in $BaTiO_3$ films via strain-induced defect dipole alignment, Adv. Mater. **26**, 6341 (2014).